

Multiwavelength study in the region of IRAS 16571-4029 and 16575-4023 sources

Baume, G.^{a,b}, Corti, M. A.^{a,c}, Borissova, J.^{d,e}, Ramirez Alegria, S.^f and Corvera, A.V.^a

^aFacultad de Ciencias Astronómicas y Geofísicas, UNLP, Argentina

^bInstituto de Astrofísica de La Plata, CONICET-UNLP, Argentina

^cInstituto Argentino de Radioastronomía, CONICET-CICPBA, Argentina

^dInstituto de Física y Astronomía, Universidad de Valparaíso, Chile

^eMillennium Institute of Astrophysics (MAS), Santiago, Chile

^fCentro de Astronomía (CITEVA), Universidad de Antofagasta, Av. Angamos 601, Antofagasta, Chile

ARTICLE INFO

Keywords:

stars: early type

stars: pre-main sequence

Galaxy: structure

ISM: HII regions

ABSTRACT

We studied the stellar populations and their associated interstellar medium structures located in the region of IRAS 16571-4029 and 16575-4023 sources, aiming to evaluate their distance and their main physical parameters. We focused our attention on the embedded cluster DBS 113 and its associated HII region RCW 116B.

For the study, optical images were obtained using wide band and narrow band filters (*ugri* and *OIII*, *OIII*_C, *H α* , *H α C*, *SII* respectively) together with infrared (*K* band) spectra for several stars in the region of DBS 113. These data were complemented with available information from the literature and photometric multi-band data from several surveys at optical (VPHAS+), infrared (2MASS, VVV, WISE) and radio (SGPS, PMN) spectral ranges. Astrometric and photometric data from GAIA DR2 in the region were also taken into account.

All the obtained spectra in DBS 113 region correspond to early type stars (OB). In general, we identified in this region 2 O-type, ~ 20 B-type stars, ~ 25 probable pre-main sequence ones, and 10 candidates to young stellar objects. We also built their stellar energy distributions ranging from 0.3 to 22 μm . We found an abnormal behaviour of the reddening law ($R_V = 4.0$) and a corresponding spectrophotometric distance from optical/infrared data consistent with the distance computed from GAIA measurements ($d \sim 2$ kpc). This value locates this cluster at the inner side of the Sagittarius-Carina Galactic arm and is different from the traditionally adopted kinematic distance of 1-1.2 kpc, based on hydrogen recombination line at millimeter wavelengths. This difference was explained by the presence of an hydrogen expanding bubble with a central velocity relative the molecular cloud. The new proposed distance value allowed to estimate more precisely the parameter values of the HII region RCW 116B and to describe the energetic balance among the emission of most massive stars, the ionization of the region and the heated dust. Regarding the IRAS 16575-4023 source, we found that the brightest star in this region is a foreground object and we also identified a set of OB stars candidates with high absorption values ($A_V \sim 23$), located behind the molecular cloud AGAL345.336+01.021.

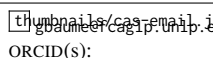
1. Introduction

A lot of smaller size star formation regions in the Milky Way have only been identified and/or have poor estimated parameters. In particular, their distances are usually based on radial velocity measurements of structures in the interstellar medium (ISM) associated with them as bubbles or HII regions (Caswell & Haynes 1987, Lebrón et al. 2001). Often, these measurements have important uncertainties (Burton 1988; Fich et al. 1989; Russeil et al. 2017) since they are based on Galactic rotation models and the results strongly depend on the adopted model. In particular, the kinematic distance estimations are usually less reliable along lines of sights near to the Galactic center (Dickey et al. 2003; Clemens 1985). Additionally, in the first and in the fourth quadrant there is ambiguity in the distance value that corresponds to each measured radial velocity. An example is the embedded cluster DBS 179 (Dutra et al., 2003) located in the direction of the H II region G347.6+0.2. A distance of 7.9 kpc was estimated by Borissova et al. (2008) based on JHK photo-

metric measurements and infrared (IR) classification of O type stars. On the other hand, using submillimeter observations, Huang et al. (1999) obtained for this region a radial velocity of $V_{LSR} = -95.2 \pm 0.1$ km s⁻¹. This value corresponds, using the Fich et al. (1989) rotation model, to the kinematic distances 6.2 ± 0.1 kpc or 10.4 ± 0.1 kpc as nearest and farthest solutions respectively. Later on Davies et al. (2012) considered a distance of 9 kpc mainly based on HI data. Therefore, it is necessary to look for independent methods to estimate the distances to these regions in order to have a better knowledge of their physical properties. This is important for outlying the general structure of our Galaxy.

It is well known, that multi-wavelength approach welds to more detailed and precise picture of the stellar populations and especially their interaction with surrounding environment. There are several public surveys, which can be used to this purpose.

In this work we focused our attention on IRAS 16571-4029 and 16575-4023 sources. They are two emerging IR sources of the molecular cloud G345.5 + 1.0 and our aim is to evaluate their main parameters to obtain a more precise picture of their physical state. The IRAS 16571-4029 source

 thumbnails/cas_email_index.html
ORCID(s):

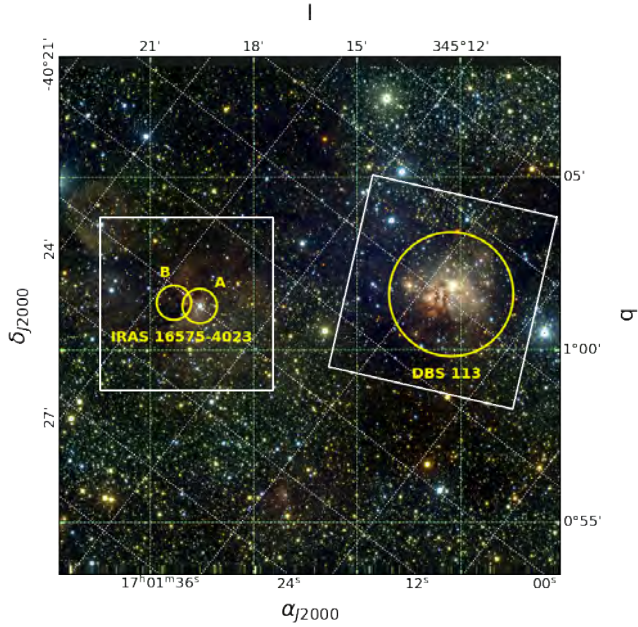


Figure 1: *JHK* false-color VVV image of working field of view (WFOV). This field is centered at $\alpha_{J2000} = 17 : 00 : 49.87$, $\delta_{J2000} = -40 : 30 : 43.7$ and covers 150×150 . DBS 113 cluster region and the two selected regions (A and B) associated with the IRAS 16575-4023 source are indicated by big yellow circles. These circles indicate the regions used to build the corresponding photometric diagrams of the IRAS sources. White rectangles represent the $5.5' \times 5.5'$ region covered by Gemini observations (see Fig. 2) and the region covered in Fig. 3.

is associated with the HII region RCW 116B and the embedded cluster DBS 113 (Dutra et al., 2003). This source has several previous studies at different spectral ranges. They include dedicated IR studies of the cluster as those carried out by Verma et al. (2003), Bik et al. (2005, 2006) and Roman-Lopes (2007) and several global works at millimetric radio waves that provided information of the region. Most of these works adopted kinematic distances from 1.8 to 2.0 kpc for the clumps associated with the molecular cloud (Bronfman et al. 1996, López et al. 2011, Wienen et al. 2015, Figueira et al. 2019). On the other hand, other works provided values ranging from 1.0 to 1.2 kpc (Caswell & Haynes 1987, Bik et al. 2005, 2006, Roman-Lopes 2007). In particular, López et al. (2011) obtained an intermediate distance value of 1.6 kpc as the average of several molecular clumps in the region and Morales et al. (2013) adopted this value for DBS 113. Figueira et al. (2019) draw attention on these discrepancies, which additionally motivated us to re-examine the distance estimations of the region.

To achieve our objectives, we employed a multi-wavelength approach based on our own observations complemented with the information provided by several surveys and the literature. In particular, we used *u* band data and IR spectroscopic observations to solve degenerated solutions in the analysis.

The paper is organised as follows. In Sect. 2 we describe the used data sources including our observations and bibli-

Table 1

Detail of scientific frames acquired using GMOS-S and selected from VSA.

Filter	Exposure times [sec.]	
	Long	Short
<i>u</i>	600 (3)	60 (3)
<i>g</i>	5 (3)	1 (3)
<i>r</i>	5 (3)	1 (3)
<i>i</i>	3 (6)	1 (3)
<i>OIII</i>	100 (3)	10 (3)
<i>OIII_c</i>	100 (3)	10 (3)
<i>H_α</i>	50 (3)	5 (3)
<i>H_{αc}</i>	50 (3)	5 (3)
<i>SII</i>	100 (3)	10 (3)
<i>J</i>	10	-
<i>H</i>	10	-
<i>K</i>	10	-

Note: Number in round brackets indicate the amount of used frames.

ographic ones. Sect. 3 presents the applied reduction procedures of our observations. Sect. 4 describes the analysis performed over the data obtaining the main stellar and ISM parameters. Finally, in Sects. 6 and 7, we discussed our results and we draw our conclusions respectively.

2. Data sources

2.1. Optical data

We used the point sources catalog of the VST Photometric *H_α* Survey of the Southern Galactic Plane and Bulge (VPHAS+; Drew et al. 2014). This catalog includes photometry at the *ugriH_α* bands. We selected those point sources located in a region of $15' \times 15'$ centered at the middle point between the IRAS 16571-4029 and 16575-4023 sources. This region was identified as our working field of view (WFOV; see Fig. 1)

Direct images were also obtained in April 2018 with the Gemini Multi-Object Spectrograph (GMOS) of Gemini-South (Cerro Pachon, Chile). In this observation run we used wide band filters *ugri* and narrow band filters *OIII*, *OIII_c*, *H_α*, *H_{αc}*, *SII* (hereafter identified as NB). See Hook et al. (2004) and Gemini webpage¹ for instrument details. The GMOS images covered a field of view (FOV) of approximately $5.5' \times 5.5'$ and were centered in the cluster DBS 113 (see Fig. 2). Three or six dithered exposures were taken per filter (see Table 1) shifted $12''$ to fill in the gaps between the detectors and to remove cosmic rays or bad pixels. Our images were taken under photometric conditions with seeing values ranging from $0.65''$ to $0.85''$. We used a 2×2 binning, giving a detector scale of $0.16''/\text{pixel}$ (Program GS-2018A-Q-323, PI: Baume).

2.2. Infrared data

We used the point sources catalog of the Two Micron All Sky Survey (2MASS; Skrutskie et al. 2006), which provides

¹<http://www.gemini.edu/>

photometric information at the JHK bands to select point sources located in the WFOV. We also obtained the JHK stacked images of the Vista Variables in the Vía Láctea (VVV; Minniti et al. 2010, Saito et al. 2012) survey. These images were downloaded from the VISTA Science Archive (VSA website²). The selected images were acquired at March 26th, 2010 and they also covered the previously indicated WFOV (see Fig. 1).

Spectroscopic images of five bright stars located in the region of DBS 113 (see Fig. 2) were additionally acquired at June 13th, 2015 as part of the 095.D-0694(A) ESO program. In this case we used the SOFI@NTT (ESO-La Silla) with a long-slit mode and a slit width of 1' to match the seeing and the medium resolution grism in the third order. This configuration allowed us to cover the whole K band (2.00–2.30 μm) with a spectral resolution of $R_\lambda = 1320$. As a measure of atmospheric absorption, we observed selected bright G type stars sharing the same airmass as the targeted stars during the middle of their observation. The resulting S/N of the obtained spectra was in the range ~ 30 –95 and their individual values are indicated in Table 4.

2.3. Additional data

We cross-correlated the previous photometric data with the information provided by the AllWISE data Release (Cutri & et al. 2013); the Gaia Data Release 2 (DR2; Gaia Collaboration et al. 2016; Brown et al. 2018). The AllWISE catalogue provides information at 3.6, 4.5, 5.8, and 8.0 μm bands, and the GAIA DR2 contains astrometric information together with photometric data at particular bands G , G_{BP} and G_{RP} . We also used colour images from the Herschel Science Archive³ obtained through *ALADIN* (Bonnarel et al., 2000). These colour images are obtained as a combination of different images obtained with the Photodetector Array Camera and Spectrometer (PACS) on board of Herschel Space Observatory at 70 and 160 μm bands.

2.4. Radio data

We used the information provided by the Southern Galactic Plane Survey (SGPS; McClure-Griffiths et al. 2005) and by the Sydney University Molonglo Sky Survey (SUMSS; Sadler & Hunstead 2001). The former is a survey of 21-cm HI spectral line emission and continuum. We used the position – velocity datacubes at HI 21-cm line, obtained with the combination data of the Australia Telescope Compact Array (ATCA) and the Parkes single dish telescopes. The angular resolution of these data is 2.2', has a channel separation of $\Delta v = 0.82 \text{ km s}^{-1}$ and a final rms noise of a single profile is $\sim 1.6 \text{ K}$ on the brightness temperature (T_b) scale. SUMSS contains radio continuum data at 843 MHz obtained with the Molonglo Observatory Synthesis Telescope (MOST) with a synthesized beam of $43'' \times 50''$ and about 1 mJy beam⁻¹ rms noise.

Table 2

Calibration coefficients used for optical and infrared observations together with the corresponding rms fit values.

<i>Coeff.</i>	$x = 1$	$x = 2$	$x = 3$	<i>rms</i>
VPHAS+ calibration				
u_x	1.96 ± 0.06	0.38	-0.14 ± 0.06	0.15
g_x	-2.88 ± 0.04	0.18	-0.14 ± 0.02	0.07
r_x	-2.75 ± 0.05	0.10	0.01 ± 0.06	0.09
i_x	-2.44 ± 0.04	0.08	-0.15 ± 0.04	0.07
ha_x	0.64 ± 0.01	r_2	-	0.06
Estimations using transmission curves				
o_x	$ha_1 - 0.306$	g_2	-	-
oc_x	$ha_1 - 1.082$	g_2	-	-
hac_x	$ha_1 - 0.089$	r_2	-	-
s_x	$ha_1 + 0.401$	r_2	-	-
2MASS calibration				
j_x	-2.79 ± 0.02	-	-0.03 ± 0.01	0.05
h_x	-2.83 ± 0.01	-	0.06 ± 0.01	0.06
k_x	-2.19 ± 0.01	-	0.12 ± 0.01	0.12

3. Reduction procedures

3.1. Photometry

Optical images obtained with GMOS were processed using GEMINI-GMOS routines within PYRAF and following the corresponding GMOS Reduction Cookbook⁴. We applied the appropriate bias and flat-field corrections using bias and flat-field images acquired from the Gemini Science Archive (GSA) and we stacked the exposures obtained with the same filter and exposure time.

As a next step, we performed the photometric measurement over the optical and IR images following a similar procedure used in Corti et al. (2016). Briefly, instrumental magnitudes were obtained using the point spread function (PSF) method (Stetson 1987) and the corresponding photometric tables were aperture-corrected for each filter to carry them to a final aperture size of 17 pixels in radius. All resulting tables were combined using DAOMASTER code (Stetson 1992), obtaining one set for $ugriH_\alpha$ + NB bands and other for JHK bands. For $ugri$ bands, the calibration in flux was done using the information of 91 common stars in the VPHAS+ catalog, whereas for the remaining NB filters, the corresponding zero point values were estimated in relation to the H_α zero point (ha_1) comparing the respective filters response. In the case of the JHK bands the calibration was carried out using the 2MASS catalog. In all this procedure we used the following transformation equations:

$$\begin{aligned}
 u_{inst} &= u + u_1 + u_2 X + u_3 (u - g) \\
 g_{inst} &= g + g_1 + g_2 X + g_3 (g - r) \\
 r_{inst} &= r + r_1 + r_2 X + r_3 (r - i) \\
 i_{inst} &= i + i_1 + i_2 X + i_3 (r - i) \\
 o_{inst} &= O + o_1 + o_2 X \\
 oc_{inst} &= Oc + oc_1 + oc_2 X
 \end{aligned}$$

²<http://horus.roe.ac.uk/vsa/>

³<http://archives.esac.esa.int/hsa/whsa/>

⁴http://ast.noao.edu/sites/default/files/GMOS_Cookbook

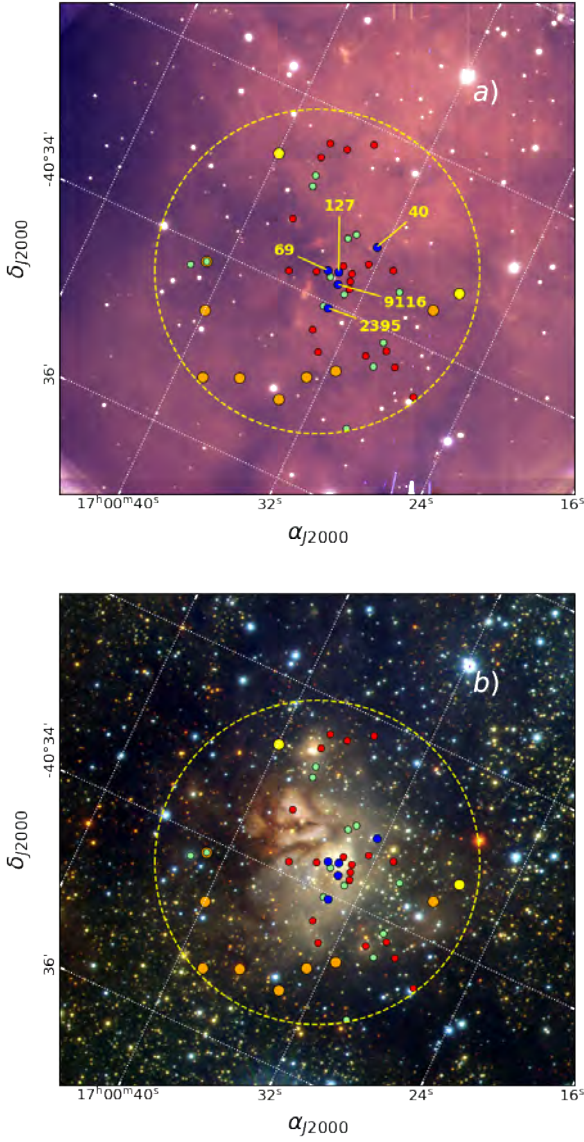


Figure 2: Color images of the region of the embedded cluster DBS 113 with the FOV covered with GMOS observations. RGB colors correspond: to $u, OIII, H_\alpha, SII$ filters in panel a and to JHK ones in panel b. Blue symbols represent stars with known spectral classification (see Fig. 4), green symbols are adopted MS stars and red ones are stars with probable IR excess. Big yellow and orange circles indicate respectively Class I and II YSOs identified using WISE colors. See Sect. 4.2 for details. Yellow slashed circle indicates the selected region for the photometric analysis. In panel a the identification of stars with spectral classification is presented.

$$\begin{aligned}
 h\alpha_{inst} &= Ha + ha_1 + ha_2 X \\
 h\alpha c_{inst} &= Hac + hac_1 + hac_2 X \\
 s_{inst} &= S + s_1 + s_2 X \\
 j_{inst} &= J + j_1 + j_3 (J - H) \\
 h_{inst} &= H + h_1 + h_3 (H - K) \\
 k_{inst} &= K + k_1 + k_3 (H - K)
 \end{aligned}$$

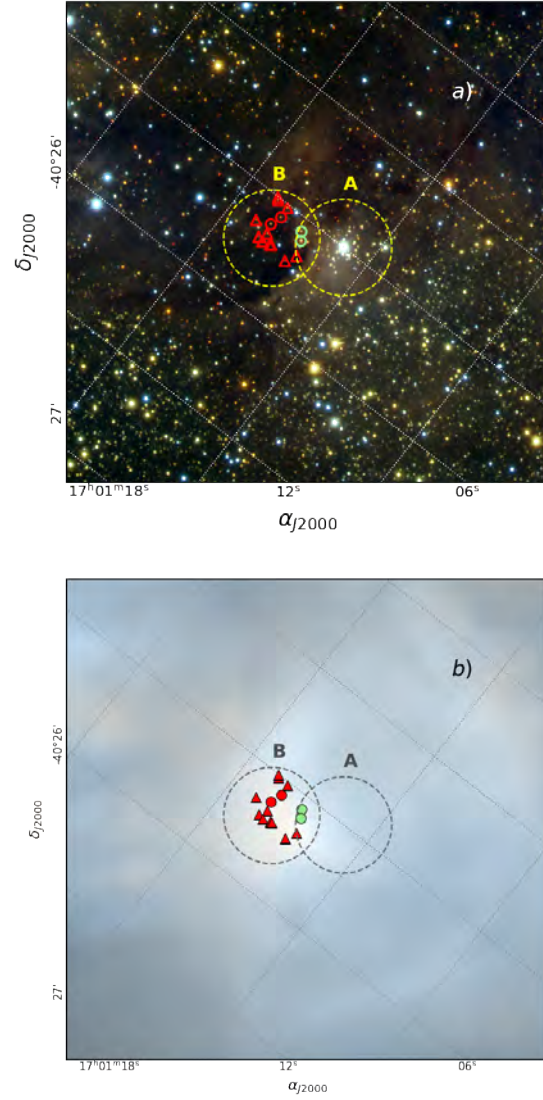


Figure 3: Color images of the region centered in the IRAS 16575-4023 source from JHK bands in panel a and from PACS/Herschel 70 μm and 160 μm bands in panel b. Symbols as in Fig. 2. Yellow slashed circles indicate both studied regions.

where $ugriH_\alpha JHK$ and $(ugrih_\alpha jhk)_{inst}$ are the VPHAS+ and 2MASS standard and instrumental magnitudes, respectively, and X is the airmass of the observation. The extinction coefficients (u_2, g_2, r_2, i_2) are given at the Gemini webpage. The other coefficients were computed using the FITPARAMS task of IRAF PHOTCAL package. The obtained values are shown in Table 2.

3.2. Astrometry

We used a similar procedure as in Baume et al. (2009). That is, since World Coordinate System (WCS) header information was only available for VVV images, we used the ALADIN tool together with the VPHAS+ and 2MASS catalogs to obtain a reliable astrometric calibration for our op-

Table 4
Selected objects in the region of IRAS 16571-4029 source.

<i>ID</i>	VPHAS+	2MASS	RL07	α_{J2000}	δ_{J2000}	<i>K</i>	SpT	<i>S/N</i>
40	1112a-11-5461112b-21-1037	17003247-4033125	9	17:00:32.5	-40:33:12.5	10.90	B4-5	29
69	1112a-11-4871112b-21-971	17003449-4033403	3	17:00:34.5	-40:33:40.2	9.29	O8-9	95
127	1112a-11-15171112b-21-976	17003386-4033382	2	17:00:33.9	-40:33:38.1	9.04	O9-B1	32, 40 *
2395	1112a-11-4481112b-21-916	-	23	17:00:33.5	-40:34:03.1	11.84	B3-4	35
9116	-	-	-	17:00:33.6	-40:33:46.0	12.53	B2-3	37

Notes: *: Each value correspond to each spectrum of this object; RL07 = Roman-Lopes (2007). Only stars with infrared spectroscopy are indicated in printed version. A complete version of this table including all the studied photometric bands and the DBS 113 members photometrically selected is available on-line at the CDS.

tical images. The resulting root mean square (rms) of the residuals in the positions were $\sim 0.10'' - 0.15''$, which is about the astrometric precision of the employed catalogs.

3.3. Spectroscopy

We followed the standard procedures to reduce the spectroscopic data, for more details see Moorwood et al. (1998), Chené et al. (2012) and Chené et al. (2013). In short, we subtracted *nodding* observations from one another to remove the bias level and sky emission lines. Then flat fielding, spectrum extraction, wavelength calibration and correction for atmospheric absorption of all spectra were done using IRAF tasks. Finally, all spectra were rectified using a low-order polynomial fit to a wavelength interval that was assumed to be pure continuum.

3.4. Final catalogs

We used the STILTS⁵ tool to manipulate tables and to crosscorrelate the optical and IR data. We then obtained four catalogs with astrometric and photometric information (*ugri* + NB + *JHK* + $W_1W_2W_3W_4$ + $GG_{BP}G_{RP}$ bands) of about 26000 objects in the WFOV. The photometric errors in the catalog are those provided by the DAOPHOT, DAOMASTER codes and the corresponding source catalogs. The full catalog (Table 3) is only available on-line at the CDS.

4. Stellar populations at IRAS sources

4.1. Spectroscopic parameters

The obtained spectra of the five stars observed in the region of the embedded cluster DBS 113 (see Sect. 2.2) are presented in Fig. 4 together with their IDs and the adopted spectral classification. We noticed that most of them present emission lines. Their spectral classification was performed using the atlas of *K* band spectra that feature spectral types stemming from optical studies (Rayner et al. 2009; Liermann et al. 2009; Meyer et al. 1998; Wallace & Hinkle 1997). We were dealing with early type stars as was expected for young star members of an embedded cluster.

Three of the stars with spectral classification (IDs 40, 69 and 127; see Table 4) were identified and measured at

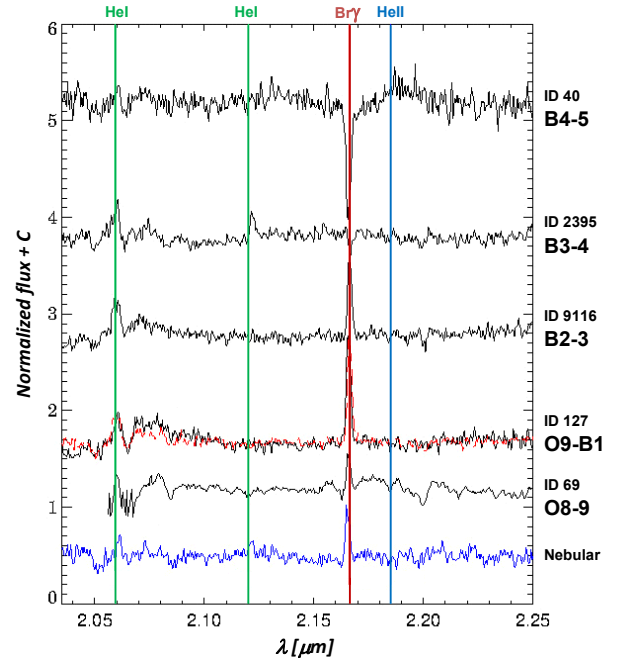


Figure 4: Stellar and nebular spectra in the DBS 113 region. Several chemical components of each star are indicated with vertical lines. The star ID and the adopted spectral type of each one is indicated on the right (see also Table 4). Notice the double spectra for star ID 127.

u band. This information allowed to estimate the reddening behavior in this direction applying the color difference method. This is, we estimated the selective absorption coefficient ($R_V = A_V/E_{B-V}$) computing the color excess ratios at *ugriJHK* bands relative to E_{g-r} , E_{g-i} and E_{u-g} . The obtained results were compared with the corresponding values given by the Cardelli et al. (1989) reddening model for a B5 V-type star (see Molina Lera et al. 2018). The used stars yield in general to large R_V values with a dependence of the adopted reference colour excess. These facts were interpreted as a consequence of emission features in their spectra (see Fig. 4) and/or uncertainties in *u* band magnitudes. Under this situation, we focused our attention on the behavior of star ID 40 (B4-5 type) and chose E_{g-i} as reference colour excess, since this star seems to present no abnormal spectral

⁵<http://www.star.bris.ac.uk/~mbt/stilts/>

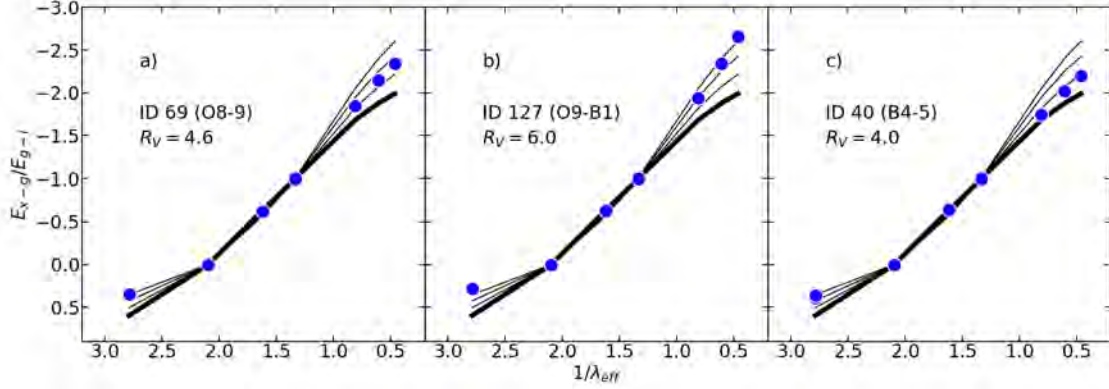


Figure 5: Colour difference method for three stars with spectral classification and u band information. Curves indicated the reddening behaviour from Cardelli et al. (1989) for $R_V = 3.1, 4.0, 5.0$ and 6.0 (from the bottom up).

Table 5

Parameters of studied IRAS sources.

IRAS	16571-4029	16575-4023 (B)
ATLASGAL	345.214+01.025	345.336+01.021
Optic	DBS 113 \equiv RCW116B	
α_{J2000}	17:00:35.0	17:01:02.0
δ_{J2000}	-40:33:44.0	-40:27:32.7
Radius [']	1.8	0.5
R_V	4.0	4.0
$E_{B-V,gr}$	1.8	5.8
A_V	~ 7	~ 23
$V_0 - M_V$	11.5 ± 0.2	11.5
d_{phot} [kpc]	2.0 ± 0.2	2
$\langle Plx \rangle$ [mas]	0.49 ± 0.07 (5)	-
d_{ast} [kpc]	2.0 ± 0.2 (5)	-
$\langle \mu_\alpha \cos(\delta) \rangle$ [mas/yr]	-0.52 ± 0.09 (7)	-
$\langle \mu_\delta \rangle$ [mas/yr]	-1.65 ± 0.07 (7)	-
$V_{R,LSR}$ [km/s] ^a	-15.24	-15.17
d_{kin} [kpc] ^a	1.9 ± 0.7	1.9 ± 0.7
$N_{Ly\ stars}$ [photons s ⁻¹]	$\sim 1.2 \cdot 10^{49}$	-
U [pc cm ⁻²]	~ 70	-

Notes: Numbers in parentheses indicate the amount of objects considered to compute the corresponding average values. **a:** ATLASGAL (Wienen et al., 2015).

features and the E_{g-i} value should be less affected by them. The results for the three stars are presented in Fig. 5. Therefore, we adopted a value of $R_V = 4.0$ as representative for the studied region and we could compute spectrophotometric color excesses and distances for the five stars with spectral classification. This procedure yield us to obtain color excesses in E_{B-V} ranging from 1.8 to 4.2 and $V_0 - M_V$ values between 10.5 to 11.9 depending on the star and the used color index. The spread in color excess values reflects the classic evidence of a young and embedded cluster, whereas the different values in distance were interpreted as a consequence of particular features in the spectral distribution of the considered stars.

4.2. Photometric analysis and object selection

To study the behavior of the stellar populations in the region of the IRAS 16571-4029 and 16575-4023 sources, we selected particular circular regions. These regions are indicated in Fig. 1. In the case of IRAS 16571-4029 source the stellar counterpart was clear, however in the case of IRAS 16575-4023 source it was hard to identify. Therefore, for this later source we considered two regions (identified as A and B). The former one was chosen based on the location of the brightest star in the area, while the later one was chosen considering the region where the molecular cloud AGAL345.336 + 01.021 (Wienen et al., 2015) was identified. The adopted centers and radius values for each circle are presented in Table 5. Then, using our catalogue, we built the color-magnitude and two-color diagrams (CMDs and TCDs, respectively) for each region. They are presented in Figs. 6, 8 and 10.

Since we were dealing with a high absorption region, the optical photometric diagrams presented a much lower amount of objects that the IR ones. However, the former allowed us to obtain a better distance estimation using the traditional main sequence (MS) fitting method. On the other hand, the upper MS has an almost vertical shape over the IR CMDs not allowing to estimate precise distance values. Notwithstanding, these latter diagrams provided an estimation of the foreground color excess of young stellar populations.

In the studied regions, all CMDs clearly revealed the presence of differential reddening. This fact hindered the estimation of colour excess and distance in this direction. Therefore, we adopted $E_{B-V} = 1.8$ as a foreground colour excess and we tested different distance values in the range obtained in the spectrophotometric analysis (see Sect. 4.1). Under each parameter set, we employed the IR diagrams to carry out a selection of different kinds of objects. It was mainly based on the colour excess range covered by stars with spectral classification ($1.8 < E_{B-V} < 5.0$) and values of the following reddening-free photometric parameters defined as:

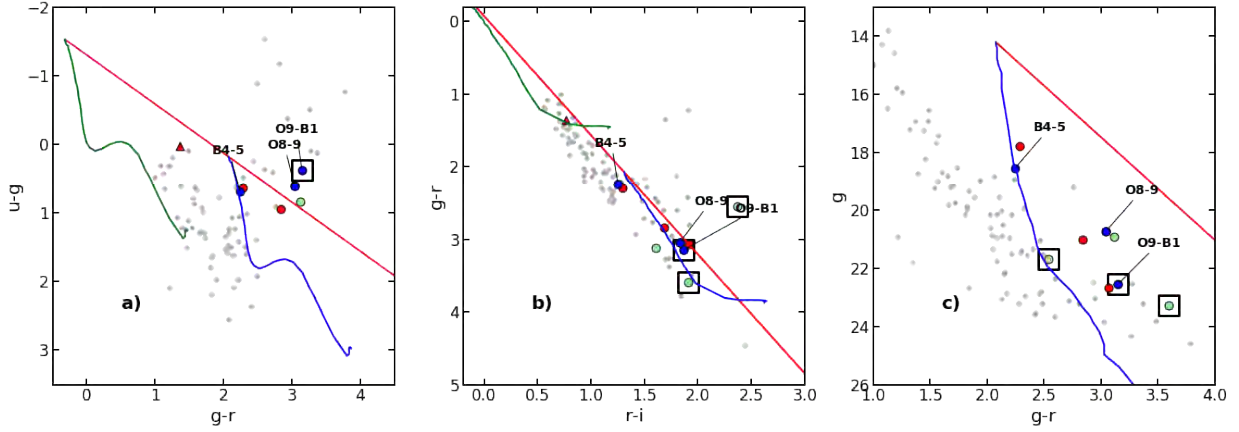


Figure 6: Optical wide band photometric diagrams for DBS 113 region. Symbols as in Fig. 2. Stars placed inside squares have some emission symptoms revealed by narrow band filter data. Light gray symbols indicate no classified stars. Most of them are field population. Green and blue curves are the ZAMS or MS (see text) shifted according to the adopted distance modulus with and without absorption/reddening, respectively. Red lines indicate the considered reddening path.

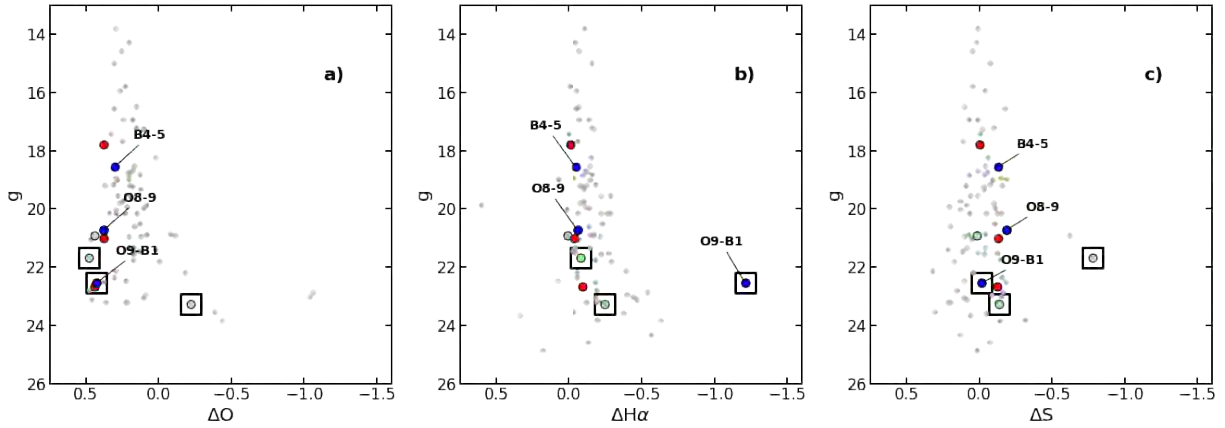


Figure 7: Narrow band index diagrams for DBS 113 region. Symbols and lines as in Fig. 6.

$$\begin{aligned}
 Q_{IR} &= (J - H) - (r_J - r_H)/(r_H - r_K) (H - K) \\
 Q_{JH} &= (J - DM) - r_J R_V (J - H) (r_B - r_V)/(r_J - r_H) \\
 Q_{HK} &= (K - DM) - r_K R_V (H - K) (r_B - r_V)/(r_H - r_K) \\
 Q_{JK} &= (J - DM) - r_J R_V (J - K) (r_B - r_V)/(r_J - r_K)
 \end{aligned}$$

where r_J , r_H and r_K are the relative absorptions ($r_x = A_x/A_V$) for JHK bands at the adopted R_V value, and DM is the considered distance modulus. Specifically, the identification of probable members of the studied regions and their classification in different categories was made with the following criteria:

- Early MS stars with colour excesses in the range above adopted. This is, objects following the conditions: $-0.1 < Q_{IR} < 0.4$, $Q_{IC} < 0.5$ and $E_{ICmin} < E_{IC} < E_{ICmax}$, with $IC = J - H$, $H - K$ and $J - K$.
- Objects with IR colour excess, identified with the same conditions used for early MS but with $Q_{IR} < -0.1$.
- Objects identified as class I and class II YSOs, follow-

ing the WISE bands color conditions given by Koenig et al. (2012)

- Probable reddened early type (OB) stars in the region B of IRAS 16575-4023 source, identified as objects with no J band data and $H - K > 2.1$,

The remaining objects were not classified and they were considered mainly as field stars.

In the case of DBS 113 region, we also employed the photometric diagrams involving NB filters computing their colour indices $O - O_C$, $H_\alpha - H_{\alpha C}$ and $S - H_\alpha$ (see Fig. 7). Therefore, we applied a Principal Components Analysis (PCA) over the tri-dimensional space of the colour indices to identify objects with line emission symptoms in at least one of these indices.

After trying several distance values, we found the most consistent solution along all the photometric diagrams adopting the $V_0 - M_V = 11.5$ for both IRAS sources (see Table 5).

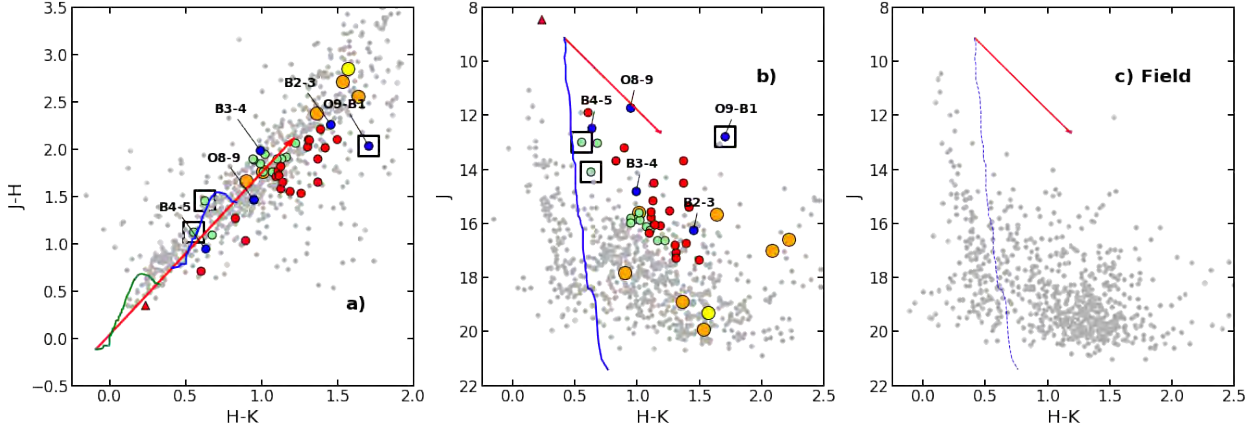


Figure 8: Infrared photometric diagrams for DBS 113 and its comparison field region. Symbols and lines as in Fig. 6.

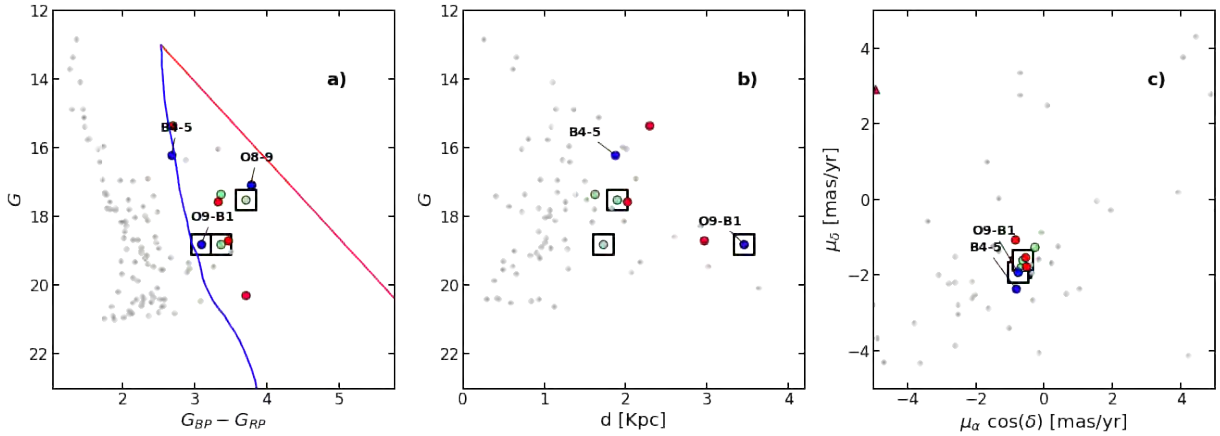


Figure 9: Photometric and astrometric diagrams for DBS 113 region from GAIA data. Symbols and lines as in Fig. 6.

4.3. Astrometric diagrams

We built the astrometric diagrams, based on GAIA DR2 data, for the point sources on each IRAS region described before.

We noticed that only some DBS 113 adopted photometrically members revealed parallax and proper motion measurements (see Fig. 9). We used the astrometric information to refine our previous photometric member selection criteria. This is, we applied a PCA over the proper motion diagram to eliminate objects placed farther than one normalized standard deviations of the mean proper motion value. The remaining objects had still large relative error values ($\sim 40\%$) in parallax, so we followed the Cantat-Gaudin et al. (2018) procedure to estimate their distance and proper motion. This is, we added $+0.029$ mas to all parallax values and then computed an error weighted average over the values ($\langle Plx \rangle$, $\langle \mu_\alpha \cos(\delta) \rangle$ and $\langle \mu_\delta \rangle$). In the case of parallaxes we selected those values with relative errors lower than 1. The obtained results are presented in Table 5. It could be noticed that the resulting relative error in parallax was lower than 20% allowing us to estimate the corresponding distance

as $d_{ast} = \langle Plx \rangle^{-1}$ (see Bailer-Jones 2015 for details). This computed distance was consistent with the already adopted one using the stellar spectra and the photometric diagrams, reinforcing our previous analysis.

In the case of IRAS 16575-4023, there are seven stars with parallax and proper motion measures in the region A, however none of them was photometrically selected as a member. In particular, the brightest star in this region (ID = 720) has a $Plx = 4.8 \pm 0.5$ mas (~ 200 pc) revealing that it is a foreground star with no physical relation with the IRAS source.

4.4. Stellar parameters

For a given distance, the parameter Q_{JH} was used to estimate the spectral types of the MS member stars, since it was little influenced by the presence of emission lines. This procedure allowed us to compute the total number ($N_{Ly\ stars}$) of ionizing photons produced by each star using the models given by Sternberg et al. (2003) and considering a Luminosity Class V. Thus, we obtained the ionization parameter of the cluster as:

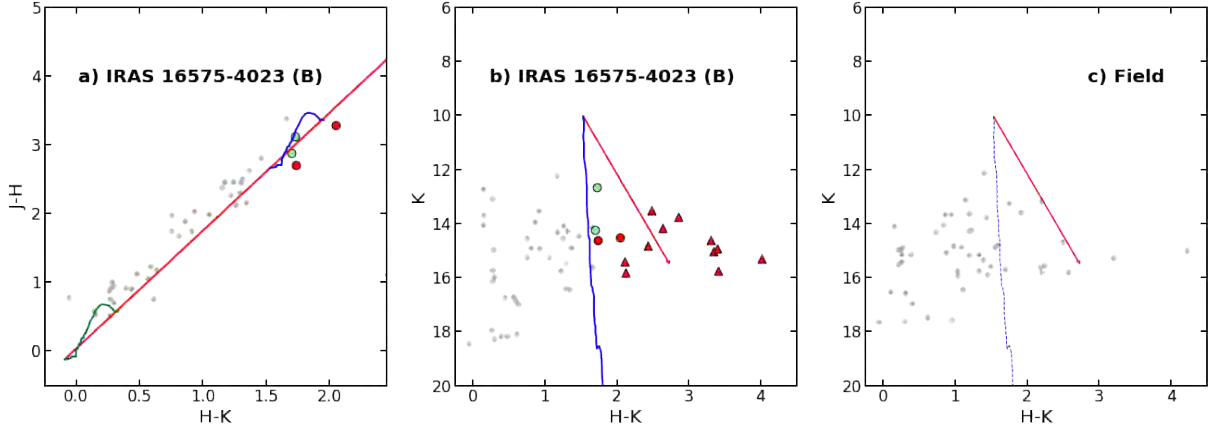


Figure 10: Infrared photometric diagrams for IRAS 16575-4023 source (region B) and its corresponding comparison field. Symbols as in Fig. 6. Red triangles represent probable early type stars

$$U[\text{pc cm}^{-2}] = \sqrt[3]{\frac{3N_{Ly \text{ stars}}}{4\pi a(2)}}$$

with $a(2) = 2.76 \times 10^{-13} [\text{cm}^3 \text{s}^{-1}]$ as the probability of recombination at all levels except the ground level. This estimations were carried out only for DBS 113 and we found that in this case the U value was mainly defined by three late O-type stars.

5. The ISM in the direction of the IRAS sources

5.1. Radio maps

Radio maps covering approximately the WFOV of the studied region (see Fig. 1) are presented in Figs. 11 and 12. Figure 11 corresponds to continuum SUMSS observations at 843 MHz and Fig. 12 shows an average of several velocity channels at HI from SGPS. These maps revealed, respectively, an evident emission and absorption signatures in the location of IRAS 16571-4029 which are consistent with a source with a continuum temperature higher than the temperature of the ISM placed in front of it. On the other hand, in the case of IRAS 16575-4023 only a faint emission centered at region A is detected at 843 MHz but no evidence of it could be found on any channel of the HI data.

Additionally, in Fig. 11 it can be noticed that both IRAS sources have almost similar shape. This fact was understood as a reflection effect of the instrumental beam and revealing that both sources could be considered with approximately circular shapes. Since the observed profiles are the result of the convolution between the real angular size (θ_{sph}) and the beam angular size ($\theta_{Ba} \times \theta_{Bb}$) of the SUMSS observations, the former could be estimated with the following relation:

$$\theta_{sph} = \sqrt{(\theta_a \theta_b) - (\theta_{Ba} \theta_{Bb})}$$

where each emission source was considered as a bidimensional gaussian distribution (Fig. 13), and θ_a / θ_b were the

corresponding measured half-power beam width (HPBW) at each principal axis. It must be notice that this procedure only yielded to a reliable result for IRAS 16571-4029 source, since for IRAS 16575-4023 we obtained a negligible angular value and we considered it as a point source.

The corresponding "flux densities" (S_ν) for each IRAS source at 843 MHz were obtained using AIPS tools. These values were computed as the difference of the total flux at the source (s_ν) and an estimation of its background level ($s_{bkg \nu}$). The corresponding background values were estimated averaging the mean flux density values at three different positions near to each source, whereas the *rms* of the flux density values (rms_{s_ν}) was considered as a measure of the noise. The corresponding angular sizes for each IRAS source are presented in Table 6.

In Fig. 14 we present a position - velocity map of the SGPS data cube at IRAS 16571-4029 location ($l = 345.2^\circ$). This figure clearly shows the presence of a minimum in bright extended from $\sim +10$ to $\sim -30 \text{ km s}^{-1}$ with a break in the range between ~ -5 to $\sim -13 \text{ km s}^{-1}$. On the other hand, the emission peaks of HI centered at ~ -10 and $\sim -20 \text{ km s}^{-1}$ are respectively consistent with the location of the Sagittarius-Carina and Scutum-Crux arms according to the Vallée (2008) model for the Galactic arms and the Fich et al. (1989) model for the Galactic rotation.

5.2. Physical ISM parameters

The 843 MHz data in the region of both IRAS sources combined with information from previous works in this region allowed to estimate several physical ISM parameters. Additionally, according to their far IR (FIR) colors (Bronfman et al., 1996), IRAS 16571-4029 and 16575-4023 sources are considered as two ultracompact H II regions. Therefore we used the indicated data and the expressions presented by Mezger & Henderson (1967) to compute the "electron density" (N_e), the "mass of ionized hydrogen" (M_{HII}) and the "emission measure" (EM). The used equations are:

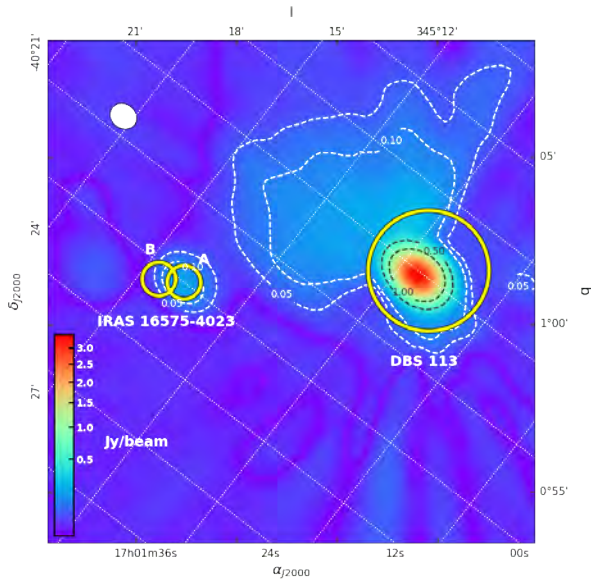


Figure 11: Radio continuum SUMSS observations at 843 MHz. Contour levels at 0.05, 0.10, 0.50 and 2.00 Jy beam^{-1} are shown. White ellipse drawn in the upper left-hand corner indicates the instrumental beam size. Yellow circles have the same meaning as in Fig. 1

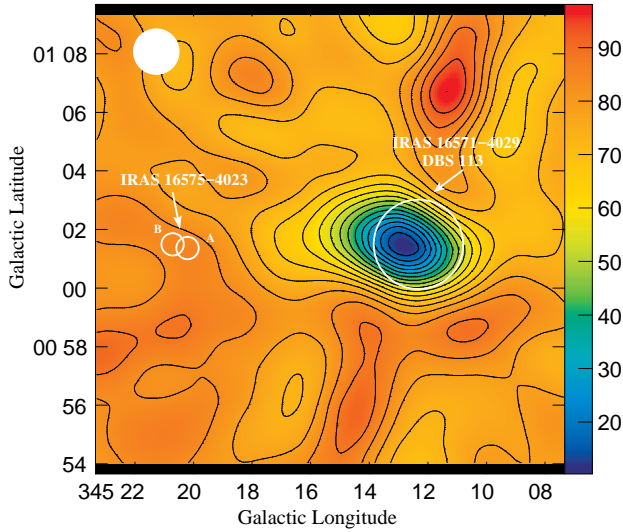


Figure 12: Average map of HI obtained with 41 radial velocity maps of the studied area (see text). Contours and colors indicate different brightness temperature values (T_b) following right bar scale. Contours vary from 5 to 100 K with a step of 5 K. White solid circle drawn in the upper left-hand corner indicates the instrumental beam size. Hollow circles have the same meaning as in Figs. 1 and 11

$$N_e[\text{cm}^{-3}] = \mu_1 a^{0.5} 635.1 (T_e [10^4 \text{K}])^{0.175} (\nu [\text{GHz}])^{0.05} \times (S_\nu [\text{Jy}])^{0.5} (d [\text{kpc}])^{-0.5} (\theta_G [\text{arcmin}])^{-1.5}$$

$$M_{\text{HII}}[M_\odot] = \mu_2 a^{0.5} 0.3864 (T_e [10^4 \text{K}])^{0.175} (\nu [\text{GHz}])^{0.05} \times (S_\nu [\text{Jy}])^{0.5} (d [\text{kpc}])^{2.5} (\theta_G [\text{arcmin}])^{1.5}$$

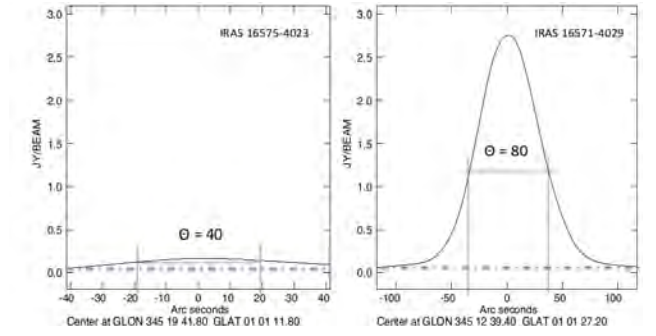


Figure 13: Flux density profiles from the SUMSS observations at 843 MHz at each IRAS source location. Dashed-point lines represents the adopted background levels. The HPBW of each profile is indicated.

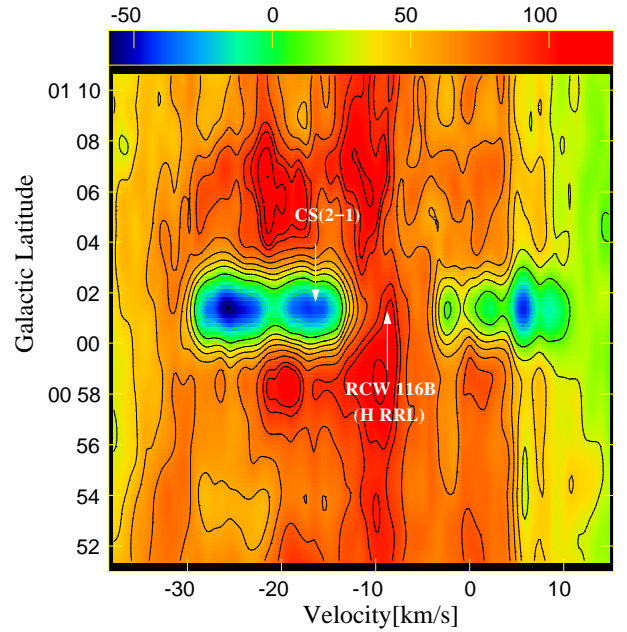


Figure 14: Position - velocity image of the HI distribution at 21 cm ($l = 345.2^\circ$). From red to blue colors are indicated the T_b gradient. Contours and colors indicate different T_b values following upper bar scale. The contours are indicated with a step of 12 K. The location of RCW 116B hydrogen RRL at -9.4 km s^{-1} and CS(2-1) lines at -15.6 km s^{-1} are also shown.

$$EM[\text{pc cm}^{-6}] = \mu_3 0.291 d [\text{kpc}] \theta_G [\text{arcmin}] (N_e [\text{cm}^{-3}])^2$$

where T_e is the electronic temperature of the HII region, d is the adopted distance and the numerical values of the factors μ_1 , μ_2 and μ_3 depend on the particular model chosen for the density distribution of the HII region. We employed the Gauss model for which $\mu_1 = 0.911$, $\mu_2 = 3.106$, $\mu_3 = 1.065$ and $a = 1$. The parameter θ_G is the angular size of the source derived assuming a Gaussian brightness temperature distribution for it. This is given by $\theta_G = \theta_{\text{sph}}/1.471$ (Mezger & Henderson, 1967) with θ_{sph} obtained as was explained in Sect. 5.1.

We also estimated the "excitation parameter" (μ). This

Table 6

Main parameters of the studied IRAS sources obtained from the 843 MHz data and complementary information from the literature. Errors computed adopting a distance error of 0.2 kpc.

	IRAS 16571-4029	IRAS 16575-4023
RCW 129B		
Parameters from SUMSS (843 MHz)		
(l,b) [°]	(345.21, +1.02)	(345.33, +1.02)
s_v [Jy beam ⁻¹]	0.6	0.07
rms_{s_v} [Jy beam ⁻¹]	$2.2 \cdot 10^{-2}$	$0.9 \cdot 10^{-2}$
s_{vbg} [Jy beam ⁻¹]	$2.1 \cdot 10^{-2}$	$1.4 \cdot 10^{-2}$
S_v [Jy]	7 ± 3	4 ± 1
θ_a ['] $\times \theta_b$ [']	1.5×1.3	0.85×0.70
θ_{sph} [']	1.2	~ 0
Physical ISM parameters		
R_s [pc]	0.35 ± 0.12	–
T_e [10^3 K]	$5.0^{(1)} - 7.6^{(2)}$	–
N_e [cm^{-3}]	$1253^{(1)} - 1347^{(2)}$	–
EM (10^5)[$pc \text{ cm}^{-6}$]	$8.4^{(1)} - 9.7^{(2)}$	–
μ [$pc \text{ cm}^{-2}$]	$41^{(1)} - 43^{(2)}$	–
M [M_\odot]	$11.3^{(1)} - 12.2^{(2)}$	–

Note: (1) Obtained adopting $T_e = 5000$ K (Caswell & Haynes, 1987); (2) Adopting $T_e = 7600$ K (Quireza et al., 2006b)

value is indicative of the number of Lyman photons absorbed by the HI and generate the HII region. The corresponding equation is:

$$\mu[pc \text{ cm}^{-2}] = R_s[pc] (N_e[cm^{-3}])^{2/3}$$

where R_s is the linear Strömngren radius corresponding to the θ_{sph} angular diameter at the adopted distance.

6. Discussion

6.1. IRAS 16571-4029 source

6.1.1. Main stellar and ISM parameters

We performed spectral classification of five stars in this region (see Sect. 4.1) and all of them could be considered as members of the cluster DBS 113. These stars revealed an abnormal R_V value in this direction. In particular, star identified as ID 127 \equiv 2MASS-J17003386-4033382 was already observed by Bik et al. (2005, 2006) using high dispersion spectroscopy and they recognized it as a triple system composed by objects identified as 16571-4029-820 (O8V-B1V), 16571-4029 1610 (O8V-B2.5V) and 16571-4029 1281 (YSO). The multiple nature would explain the very abnormal R_V value found for this star (see Fig. 5). Our spectroscopic data, with lower spectral resolution allowed to separate two components (see Fig. 4) and revealed an strong Br γ emission line. In general, our spectroscopic and photometric analysis at optical/IR bands allowed us to recognize the presence of an important amount of early MS stars (2 O-type and \sim 20 B-type) and \sim 25 probable PMS stars. Additionally, our study with Spitzer data revealed 2 Class I, 8 Class II YSO

Table 7

Compilation of kinematic information in the direction of IRAS 16571-4029 \equiv G345.23+1.03 source.

Line	$V_{R,LSR}$ [km s ⁻¹]	ΔV [km s ⁻¹]	Ref.
H109 α	-9.40 ± 1.80	28.50 ± 3.60	1,2
H	-11.54 ± 0.13	29.11 ± 0.39	4
⁴ He	-11.26 ± 0.39	21.69 ± 1.43	4
CS(2-1)	-15.60 ± 0.52	4.90 ± 0.52	3
CS(7-6)	-15.03 ± 0.03	3.12 ± 0.07	5
CII	-16.20 ± 0.51	4.44 ± 1.18	4
HCN(4-3)	-14.69 ± 0.12	5.65 ± 0.41	5

Note: (1) Wilson et al. (1970); (2) Caswell & Haynes (1987); (3) Bronfman et al. (1996) and adopted errors correspond to the velocity resolution; (4) Quireza et al. (2006a); (5) Liu et al. (2016)

candidates.

The cross correlation procedure performed among our optical/IR photometric data (*ugriJHK*) and those data available on several catalogues (2MASS, Spitzer, WISE) yielded to obtain the stellar energy distributions (SEDs) ranging from 0.3 to 22 μ m for selected objects in the region of IRAS 16571-4029 source. In this procedure we used the corresponding zero point fluxes given at NASA/IPAC Infrared Science Archive⁶. The obtained SEDs are presented in Fig. 15 and their comparison showed that adopted MS stars and PMS candidates (three upper panels) present a maximum at about 1.5-2 μ m and then a decreasing behaviour. On the other hand, it is possible to note that the adopted objects identified as Class I YSO (lower panel, yellow symbols) present a rising energy distribution, whereas objects identified as Class II YSO (lower panel, orange symbols) present a minimum at about 5-6 μ m and then a stable or rising shape at longer wavelengths.

Regarding the ISM parameter values for IRAS 16571-4029 source, they are presented in Table 6 and were computed following the guidelines given at Sect. 5.2. In particular, T_e was already computed by Caswell & Haynes (1987) ($T_e \simeq 5000$ K) and by Quireza et al. (2006b) ($T_e \simeq 7600$ K) from observations at 5 and 8.6 GHz respectively, where the plasma of the region is optically thin. We used both T_e values to estimate the ISM parameters and they are presented in Table 6.

6.1.2. Distance to the source

Since we had available spectroscopic classification and GAIA astrometric data for several stars in the region, it was possible to estimate spectrophotometric and trigonometric distances. Additionally, the SGPS HI data allowed us to obtain a kinematic distance.

To understand more precisely the HI kinematic behavior in this direction, we obtained the HI emission and absorption profiles performing the disjoin of the Galactic background emission to the small scale structures around and on the compact H II region. This task was done using a similar

⁶<https://irsa.ipac.caltech.edu>

Table 8
OB candidate objects in the region of IRAS 16575-4023 (B) source

ID	2MASS	GLIMPSE	α_{J2000}	δ_{J2000}	J	H	K
7992	17010017-4027289	G345.3356+01.0279	17:01:00.2	-40:27:28.9	17.16 ± –	15.99 ± 0.02	13.52 ± 0.02
8061	17010073-4027449	G345.3332+01.0238	17:01:01.0	-40:27:44.9	18.84 ± 0.07	15.95 ± 0.02	14.26 ± 0.02
8064	17010081-4027293	G345.3366+01.0263	17:01:00.8	-40:27:29.4	19.84 ± 0.12	16.56 ± 0.03	14.51 ± 0.03
8110	17010114-4027483	G345.3333+01.0222	17:01:01.2	-40:27:48.1	17.51 ± 0.02	14.39 ± 0.02	12.66 ± 0.02
8117	17010143-4027269	G345.3385+01.0251	17:01:01.4	-40:27:27.0	19.08 ± 0.06	16.37 ± 0.02	14.63 ± 0.02
8122	17010016-4027212	G345.3372+01.0293	17:01:00.2	-40:27:21.2	18.16 ± –	16.64 ± 0.03	13.78 ± 0.04

Note: A complete version of this table including all the studied photometric bands is available on-line at the CDS.

procedure to that given by Kothes & Kerton (2002). Basically we convolved each velocity channel of the HI data cube with a gaussian beam of FWHM = 10.0' to obtain the emission profiles and the subtraction between the original data and its smoothed version to get the absorption profiles. The resulting profiles in the direction of the absorption minimum near the IRAS 16571-4029 source are presented in Fig. 16a. In this figure it is clear the location of the tangential velocity ($V_T = -150$ km s⁻¹) at the emission feature with the largest negative velocity value and the presence of two main absorption features with an upper velocity value of ~ -30 km s⁻¹. In particular, the fact that there are no absorption features up to the tangential velocity reveals they are caused closer than the tangential point in this direction.

A roughly and traditional analysis of Figs. 14 and 16 indicate that the corresponding radial velocity value of the studied HII region is given by the highest negative value of the absorption feature (~ -30 km s⁻¹). However, this value is inconsistent with those given in previous studies at radio wavelength of this region. A compilation of the velocity values are presented in Table 7, where it can be remarked the difference in the velocity values between those obtained from hydrogen radio recombination lines (~ -9 and ~ -11 km s⁻¹ with $\Delta V \sim 30$ km s⁻¹) and the resulting from molecular studies (~ -15 km s⁻¹ with $\Delta V \sim 5$ km s⁻¹). Therefore Fig. 14 shows an absorption component up to ~ 20 km s⁻¹ beyond the hydrogen RRL velocity. Using the Galactic rotation model of Fich et al. (1989) and adopting the corresponding nearest distances, the presented V_R values: -9, -11, -15 and -30 km s⁻¹ yielded respectively to kinematic distance values of 1.25, 1.45, 1.95 and 3.2 kpc. These discrepancies could be understood as a consequence of local departures from the rotation curve. It would not be strange since we are working at Galactic longitude values close to the Galactic center direction and we also could be dealing with somewhat turbulent flows (Jones & Dickey, 2012). Besides this, the possible presence of streaming motions could induce local kinematic distance ambiguities (Fish et al., 2003),

Under these circumstances, the kinematic analysis did not seem to provide a reliable way to estimate the distance to the IRAS 16571-4029 source and we adopted the value computed from GAIA data which is consistent with the spectrophotometric one (see Table 5). Additionally, with this distance value, the kinematic data could be reanalyzed taking into account that the ΔV value of ~ 28 km s⁻¹ indicated

by Wilson et al. (1970) is comparable with the complete extension, from +10 to -30 km s⁻¹, of the minimum presented in Fig. 14. These values could be understood as due to turbulent movements and/or an hydrogen expanding bubble ($V_{Rexp} \sim V_{Fexp} \sim 20$ km s⁻¹) around a central value of ~ -10 km s⁻¹ given by the HI RRLs and this would be shifted by a peculiar velocity of about 5 km s⁻¹ from the ~ -15 km s⁻¹ given by the molecular cloud velocity measurements that correspond with a kinematic distance near to 2 kpc (see Fig. 16b for an schematic representation of this scenario). These kind of behaviour was already found on other HII regions by Caswell & Haynes (1987) and Kothes & Kerton (2002). In fact, Morales et al. (2013) already identified DBS 113 as a *partially* embedded cluster since the peak at the submillimetric observations is significantly shifted in location from the cluster itself, giving an additional support to the idea of a cluster with a kinematic behavior different to that one of the molecular cloud.

6.1.3. Energetic balance in the source

The estimated ISM parameters for the IRAS 16571-4029 source revealed it as a compact or classical HII region and following Kurtz et al. (1994) the ionization-bounded case is probably a very good assumption but it is not a dust-free nebula. Therefore it is possible to compare the energy needed to excite the HII region with that provided by the brightest stars of DBS 113 from the values found for the excitation parameter (μ , see Sect. 5.2) and the ionization parameter (U , see Sect. 4.4). The ratio $U/\mu \approx 1.7 > 1$ indicated that cluster stars produce enough radiant energy to generate the HII region. Since $U \propto N_{Ly\ stars}^{1/3}$ then:

$$\frac{U}{\mu} = \left(\frac{N_{Ly\ stars}}{N_{Ly\ HII}} \right)^{1/3}$$

where $N_{Ly\ HII}$ indicates the amount of Lyman photons required to generate the observed HII region, resulting to be $N_{Ly\ HII} \sim 2.5 \cdot 10^{48}$ photons s⁻¹. On the other hand, there is ~ 80 % of the stellar energy ($1 - (\mu/U)^3$) generating an increase in the temperature of the interstellar dust. It must be noticed that in the previous computation dust absorption would include both the ISM component and the probable circumstellar ones Kurtz et al. (1994).

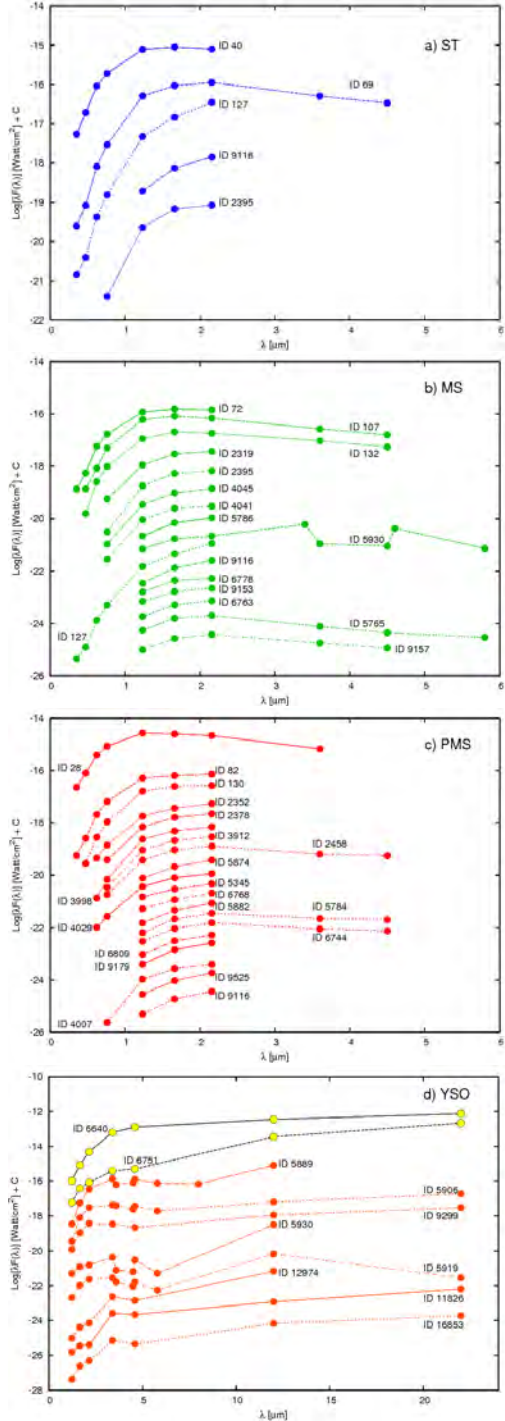


Figure 15: The SEDs of selected objects considered members of DBS 113. Symbols along the panels have the same meaning as in Fig. 6

6.2. IRAS 16575-4023 source

This IRAS source is a very poor object and there is almost no information about it. The source was only identified as an HII region according to Bronfman et al. (1996), and Volk et al. (1991) obtained a unique and unusual infrared spectrum with a possible absorption at $11.3 \mu\text{m}$. As was previously indicated, to study this source, we selected two

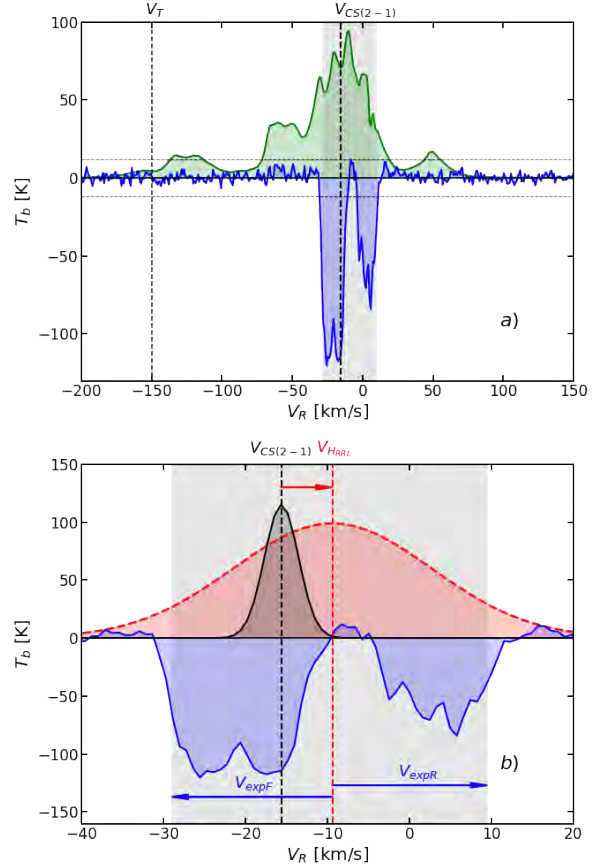


Figure 16: a) Emission (green) and absorption (blue) HI profiles at the center of the RCW 116B region covering almost all the velocity channels. Vertical slashed lines indicate the tangential velocity ($V_T = -150 \text{ km s}^{-1}$) and the CS molecular line ($V_{CS} = -15.6 \text{ km s}^{-1}$). The horizontal lines represent $\Delta T_b = 12 \text{ K} \sim 5 \text{ rms}_{\text{bkg}}$ b) Absorption (blue) profile together with a schematic representation of the CS lines (black fill curve) and HI RRL (slashed red curve) as two gaussian profiles with arbitrary height. Shadow regions in both panels indicate the velocity range for absorption features ($-29 \text{ km s}^{-1} < V_R < +9 \text{ km s}^{-1}$). See text for arrows meaning.

regions: A and B. The stellar population in region A presents an overdensity of faint stars which does not seem related with the IRAS source, however in this location is the peak of the radio continuum SUMSS observations at 843 MHz. Region B, revealed a spatial concentration of very faint and red objects consistent with high reddened early type stars (OB; see CMDs in Fig. 10 and Table 8) located behind the molecular cloud AGAL345.336 +01.021. This location is revealed in the PACS/Herschel image (see Fig. 10b) as the center of a clear bubble of about $2'$ in radius reinforcing the presence of early stars. On the other hand, the adopted distance for these stars ($\sim 2 \text{ kpc}$) agrees with the kinematic one of 1.9 kpc indicated by Wielen et al. (2015) for the molecular cloud. Additionally, the research of CS(2-1) lines done by Bronfman et al. (1996) at this direction provided a value of V_R (LSR) $= -14.5 \text{ km s}^{-1}$ with a $\Delta V = 2.8 \text{ km s}^{-1}$. With the use of the Galactic rotation model of Fich et al. (1989) we could also

estimate for it a distance of $d = 1.9$ kpc, adopting the nearest distance as was the case of DBS 113.

7. Conclusions

We studied the IRAS 16571-4029 and 16575-4023 sources located in the fourth Galactic quadrant of the Milky Way plane through a multiwavelength and multitechnique approach. We focused our attention on embedded cluster DBS 113 associated with IRAS 16571-4029 since this region appear as more relevant and there were contradictions about its distance. We used then several methods to estimate this value and we found the most probable one is 2 kpc. This value is consistent with previous estimations based on studies of the associated molecular cloud G345.5+1.0 and located this star formation region at the inner side of the Sagittarius-Carina Galactic arm. A more reliable distance estimation allowed us to obtain better estimations of the physical parameters of the region. In particular, from the relationship studied between U and μ parameters yielded to conclude that the region is limited by density and 80 % of Lyman photons produced by the early stars are consumed by the dust. Additionally, our kinematic study at this direction revealed a particular behaviour of the gas in this part of the Galaxy, showing much larger radial velocity values (in absolute terms) at the location of the cluster and HII region that those expected from the usual rotation model.

It must be notice the importance to use stellar spectroscopic classification along with u band data to obtain a better estimation of the reddening law for this cluster. Our photometric and spectroscopic analysis using optical/IR bands was useful to identify early stars and sources with IR excess in this region. Additionally, by using Spitzer FIR data we could classify several objects as YSOs.

Regarding IRAS 16575-4023 source, we found that the brightest star in the region is a field foreground one according to GAIA DR2 data and we identified a probably very faint and reddened young stellar population responsible of the HII region and an IR bubble revealed at 70 and 160 μm bands. Found young stellar candidates deserve a future spectroscopic follow up to confirm their nature.

Acknowledgements

G.B and M.A.C. acknowledge support from CONICET (PIPs 112-201701-00055 and 112-201701-00507). S.R.A. acknowledges the support by the FONDECYT Iniciación project No11171025 and the CONICYT PAI "Concurso Nacional Inserción de Capital Humano Avanzado en la Academia 2017" project PAI 79170089. Support for J.B. is provided by the Ministry of Economy, Development, and Tourism's Millennium Science Initiative through grant IN 120009, awarded to The Millennium Institute of Astrophysics, The authors are much obliged for the use of the NASA Astrophysics Data System, of the SIMBAD database and ALADIN tools (CDS, France). This publication was based on: a) Observations and data products from observations made with ESO Telescopes

at the La Silla or Paranal Observatories; b) Observations obtained at the Gemini Observatory, which is operated by the Association of Universities for Research in Astronomy, Inc., under a cooperative agreement with the NSF on behalf of the Gemini partnership: the NSF (USA), NRC (Canada), CONICYT (Chile), Sec. de Ciencia, Tecnología e Innovación Productiva (Argentina), Min. da Ciência, Tecnologia e Inovação (Brazil), and KASSI (Republic of Korea); c) The 2MASS, which is a joint project of the University of Massachusetts and the IPAC/California Institute of Technology, funded by the NASA and the NSF; d) Data products from the WISE, which is a joint project of the University of California, Los Angeles, and the JPL/California Institute of Technology, and is funded by the NASA; e) Data from the ESA mission *Gaia*, processed by the *Gaia* DPAC. Funding for the DPAC has been provided by national institutions, in particular the institutions participating in the *Gaia* Multilateral Agreement; f) The SGPS is a project with images obtained at high resolution using the Australia Telescope Compact Array and the Parkes Radio Telescope; g) The SUMSS is a radio imaging survey carried out with the Molonglo Observatory Synthesis Telescope (MOST), Australia.

References

- Bailer-Jones C. A. L., 2015, *PASP*, 127, 994
 Baume G., Carraro G., Momany Y., 2009, *MNRAS*, 398, 221
 Bik A., Kaper L., Hanson M. M., Smits M., 2005, *A&A*, 440, 121
 Bik A., Kaper L., Waters L. B. F. M., 2006, *A&A*, 455, 561
 Bonnarel F., et al., 2000, *A&AS*, 143, 33
 Borissova J., Ivanov V. D., Hanson M. M., Georgiev L., Minniti D., Kurtev R., Geisler D., 2008, *A&A*, 488, 151
 Bronfman L., Nyman L.-A., May J., 1996, *A&AS*, 115, 81
 Brown A. G. A., et al., 2018, *A&A*, 616, A1
 Burton W. B., 1988, The structure of our Galaxy derived from observations of neutral hydrogen. pp 295–358
 Cantat-Gaudin T., et al., 2018, preprint, (arXiv:1810.05494)
 Cardelli J. A., Clayton G. C., Mathis J. S., 1989, *ApJ*, 345, 245
 Caswell J. L., Haynes R. F., 1987, *A&A*, 171, 261
 Chené A.-N., et al., 2012, *A&A*, 545, A54
 Chené A.-N., et al., 2013, *A&A*, 549, A98
 Clemens D. P., 1985, *ApJ*, 295, 422
 Corti M. A., et al., 2016, *A&A*, 588, A63
 Cutri R. M., et al. 2013, *VizieR Online Data Catalog*, 2328
 Davies B., de La Fuente D., Najarro F., Hinton J. A., Trombly C., Figer D. F., Puga E., 2012, *MNRAS*, 419, 1860
 Dickey J. M., McClure-Griffiths N. M., Gaensler B. M., Green A. J., 2003, *ApJ*, 585, 801
 Drew J. E., et al., 2014, *MNRAS*, 440, 2036
 Dutra C. M., Bica E., Soares J., Barby B., 2003, *A&A*, 400, 533
 Fich M., Blitz L., Stark A. A., 1989, *ApJ*, 342, 272
 Figueira M., López-Calderón C., Bronfman L., Zavagno A., Hervías-Caimapo C., Duronea N., Nyman L.-A., 2019, *A&A*, 623, A141
 Fish V. L., Reid M. J., Wilner D. J., Churchwell E., 2003, *ApJ*, 587, 701
 Gaia Collaboration et al., 2016, *A&A*, 595, A1
 Hook I. M., Jørgensen L., Allington-Smith J. R., Davies R. L., Metcalfe N., Murowinski R. G., Crampton D., 2004, *PASP*, 116, 425
 Huang M., et al., 1999, *ApJ*, 517, 282
 Jones C., Dickey J. M., 2012, *ApJ*, 753, 62
 Koenig X. P., Leisawitz D. T., Benford D. J., Rebull L. M., Padgett D. L., Assef R. J., 2012, *ApJ*, 744, 130
 Kothes R., Kerton C. R., 2002, *A&A*, 390, 337
 Kurtz S., Churchwell E., Wood D. O. S., 1994, *ApJS*, 91, 659
 Lebrón M. E., Rodríguez L. F., Lizano S., 2001, *ApJ*, 560, 806

- Liermann A., Hamann W.-R., Oskinova L. M., 2009, *A&A*, 494, 1137
- Liu T., et al., 2016, *ApJ*, 829, 59
- López C., Bronfman L., Nyman L.-Å., May J., Garay G., 2011, *A&A*, 534, A131
- McClure-Griffiths N. M., Dickey J. M., Gaensler B. M., Green A. J., Haverkorn M., Strasser S., 2005, *ApJS*, 158, 178
- Meyer M. R., Edwards S., Hinkle K. H., Strom S. E., 1998, *ApJ*, 508, 397
- Mezger P. G., Henderson A. P., 1967, *ApJ*, 147, 471
- Minniti D., et al., 2010, *New Astron.*, 15, 433
- Molina Lera J. A., Baume G., Gamen R., 2018, *MNRAS*, 480, 2386
- Moorwood A., Cuby J.-G., Lidman C., 1998, *The Messenger*, 91, 9
- Morales E. F. E., Wyrowski F., Schuller F., Menten K. M., 2013, *A&A*, 560, A76
- Quiroza C., Rood R. T., Balsa D. S., Bania T. M., 2006a, *ApJS*, 165, 338
- Quiroza C., Rood R. T., Bania T. M., Balsa D. S., Maciel W. J., 2006b, *ApJ*, 653, 1226
- Rayner J. T., Cushing M. C., Vacca W. D., 2009, *ApJS*, 185, 289
- Roman-Lopes A., 2007, *A&A*, 471, 813
- Russeil D., Zavagno A., Mège P., Poulin Y., Molinari S., Cambresy L., 2017, *A&A*, 601, L5
- Sadler E. M., Hunstead R. W., 2001, in Clowes R., Adamson A., Bromage G., eds, *Astronomical Society of the Pacific Conference Series Vol. 232, The New Era of Wide Field Astronomy*. p. 53
- Saito R. K., et al., 2012, *A&A*, 537, A107
- Skrutskie M. F., et al., 2006, *AJ*, 131, 1163
- Sternberg A., Hoffmann T. L., Pauldrach A. W. A., 2003, *ApJ*, 599, 1333
- Stetson P. B., 1987, *PASP*, 99, 191
- Stetson P. B., 1992, in Worrall D. M., Biemesderfer C., Barnes J., eds, *Astronomical Society of the Pacific Conference Series Vol. 25, Astronomical Data Analysis Software and Systems I*. p. 297
- Vallée J. P., 2008, *AJ*, 135, 1301
- Verma R. P., Ghosh S. K., Kulkarni V. K., Ojha D. K., 2003, *Bulletin of the Astronomical Society of India*, 31, 399
- Volk K., Kwok S., Stencel R. E., Brugel E., 1991, *ApJS*, 77, 607
- Wallace L., Hinkle K., 1997, *ApJS*, 111, 445
- Wiener M., et al., 2015, *A&A*, 579, A91
- Wilson T. L., Mezger P. G., Gardner F. F., Milne D. K., 1970, *A&A*, 6, 364